J Adv Ceram

Research Article

Enhanced luminescence, thermal stability, and scintillation performance in $Zn_2SiO_4:Mn^{2+}$ phosphors via a lattice modification strategy based on Mg^{2+} co-doping

Simin Yu, Guanlin He, Xinglin Jiang, Hai Guo✉

Cite this article: Yu S, He G, Jiang X, et al. *J Adv Ceram* 2026, **15**: 9221352. https://doi.org/10.26599/JAC.2026.9221352

ABSTRACT: Mn^{2+}-based inorganic scintillation phosphors have attracted considerable attention due to their tunable optical properties, low toxicity, and high luminescent efficiency. However, their practical applications commonly suffer from extreme thermal quenching. In this paper, a lattice modification strategy involving the introduction of Mg^{2+} into $Zn_2SiO_4:Mn^{2+}$ phosphors is proposed to improve the thermal stability and luminescence of Mn^{2+}. The X-ray excited luminescence (XEL) intensity of $Zn_2SiO_4:Mn^{2+},Mg^{2+}$ phosphors is 493% of that of $Bi_4Ge_3O_{12}$ powders and is enhanced by 2 times compared to that of $Zn_2SiO_4:Mn^{2+}$ phosphors. The corresponding flexible film exhibits a high spatial resolution of 20 lp/mm and excellent stability after immersion in H_2O or CH_3CH_2OH for 10 d. In addition, the $Zn_2SiO_4:Mn^{2+},Mg^{2+}$ phosphors present unique anti-thermal quenching luminescence. Its XEL intensity at 483 K is 126% of that at 303 K. Through thermoluminescence analysis, the anti-thermal quenching of Mn^{2+} can be explained by the fact that Mg^{2+} incorporation effectively reduces structural defects induced by Mn^{2+}–Zn^{2+} substitution. This work confirms the scintillation potential of $Zn_2SiO_4:Mn^{2+},Mg^{2+}$ phosphors and offers a meaningful strategy for developing novel scintillators for advanced X-ray imaging applications.

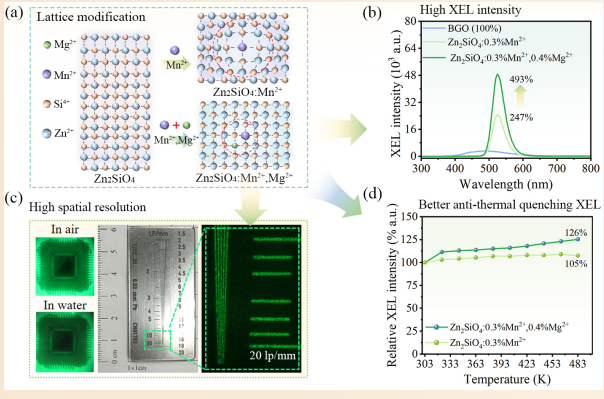

KEYWORDS: $Zn_2SiO_4:Mn^{2+},Mg^{2+}$ phosphors; scintillator; lattice modification; anti-thermal quenching; X-ray imaging

1 Introduction

Scintillators, which convert high-energy radiation (e.g., X-rays and γ-rays) into ultraviolet or visible light, are fundamental to modern applications such as radiation detection, medical imaging, and safety monitoring [1–6]. Currently, commercial bulk scintillators, including single crystals (e.g., NaI, $Bi_4Ge_3O_{12}$ (BGO)), transparent ceramics (e.g., $Y_3Al_5O_{12}:Ce^{3+}$ (YAG:Ce^{3+})), and glass, have been widely developed and exhibit considerable light yield [7–10]. However, their application in advanced scintillation fields is limited by poor moldability and high preparation costs. In addition, some of these materials suffer from inadequate stability, which can lead to luminescence degradation after prolonged exposure to high-temperature or high-humidity environments [7,11]. In contrast, scintillation powders, including inorganic phosphors, perovskites, and metal-organic frameworks, possess high plasticity and cost-effective preparation [4,12–14]. They can be fabricated into fluorescent coatings or films and readily deposited onto various surfaces for imaging applications where commercial bulk scintillators are impractical. Therefore, the development of inorganic phosphors with high scintillation performance and thermal stability is of great importance for advanced scintillation applications [15–17].

Among the diverse types of scintillation powders, Mn^{2+}-based inorganic scintillation phosphors have been widely investigated due to their tunable optical properties, low toxicity, and high luminescent efficiency [15,18,19]. The unique $3d^5$ electron configuration of Mn^{2+} couples strongly with the crystal lattice, resulting in broadband emission that ranges from green to infrared, depending on the host material [20,21]. Nevertheless, due to strong electron-phonon coupling, the luminescence of Mn^{2+} is highly sensitive to even slight lattice vibrations, which leads to severe thermal quenching during heating [22–24]. In addition, the luminescence of Mn^{2+} may be closely related to the local coordination environment. A high density of defects within materials may also induce significant thermal quenching of Mn^{2+} emission [25–27]. Therefore, developing effective strategies to improve the luminescence stability of Mn^{2+} in Mn^{2+}-based scintillation phosphors remains a major challenge for practical applications.

Department of Physics, Zhejiang Normal University, Jinghua 321004, China.

✉ Corresponding author. E-mail: ghh@zjnu.cn

Received: April 29, 2026; Revised: June 23, 2026; Accepted: July 16, 2026

As mentioned above, the luminescent behavior of Mn^{2+} is significantly influenced by host material, which requires careful consideration. Compared with germanates and gallates, silicates usually possess less intrinsic defects and exhibit weak self-activated luminescence, which avoids potential optical interference from host on Mn^{2+} emission [28,29]. In addition, many silicates offer high stability and low cost, making them promising candidates for large-scale production. Zn_2SiO_4, a common host for commercial phosphors, was chosen as the host material in this study. When Mn^{2+} is introduced, it can easily substitute for Zn^{2+} site due to their comparable ionic radii, resulting in bright green emission. Although the photoluminescence (PL) properties of Zn_2SiO_4:Mn^{2+} have been widely reported, investigations into its scintillation performance remain relatively limited. Currently, Jarý *et al.* [30] reported Zn_2SiO_4:Mn^{2+} glass-ceramics with relatively considerable X-ray excited luminescence (XEL). Diana *et al.* [31] investigated the thermoluminescence (TL) of Zn_2SiO_4:Mn^{2+} phosphors under X-ray irradiation. However, their studies on scintillation performance lack further optimization and comprehensive exploration (Table S1 in the Electronic Supplementary Material (ESM)). Generally, radiative recombination defects (e.g., vacancies) can act as trap centers that compensate for luminescence loss during heating and improve thermal stability [32]. Nevertheless, a high concentration of nonradiative recombination defects (e.g., interstitials and structural defects) may reduce XEL intensity of material [33]. The substitution of Mn^{2+} for Zn^{2+} avoids the formation of cation or anion vacancies, which preserves the structural integrity of lattice. However, this substitution induces local lattice expansion, as the ionic radius (r) of Mn^{2+} (r = 0.66 Å) is slightly larger than that of Zn^{2+} (r = 0.60 Å). Such expansion may introduce nonradiative recombination centers or structural defects, which can reduce the luminescent efficiency and thermal stability of Mn^{2+} [25,34,35]. To overcome this drawback, a smaller-sized Mg^{2+} (r = 0.57 Å) is intentionally incorporated to replace Zn^{2+}. As a result, the lattice contraction induced by Mg^{2+} can compensate for lattice expansion caused by Mn^{2+} doping, thus suppressing the formation of structural defects. Ivanova *et al.* [36] demonstrated the effectiveness of this strategy in enhancing PL intensity. Nevertheless, the effect of Mg^{2+} incorporation on the scintillation performance of Mn^{2+} remains unexplored (Table S1 in the ESM).

Therefore, the effect of Mg^{2+} incorporation on the scintillation properties of Mn^{2+} is systematically explored in this work. Remarkably, upon Mg^{2+} incorporation, the XEL intensity of Zn_2SiO_4:Mn^{2+}, Mg^{2+} phosphors reaches 493% of that of BGO powders and is twice as high as that of Zn_2SiO_4:Mn^{2+} phosphors. The corresponding flexible film exhibits excellent spatial resolution (20 lp/mm) along with good physicochemical stability in H_2O and CH_3CH_2OH. Moreover, the integrated XEL intensity of Zn_2SiO_4:Mn^{2+},Mg^{2+} phosphors at 483 K remains at 126% of that at 303 K, demonstrating exceptional anti-thermal quenching luminescence. These results confirm the potential of Zn_2SiO_4:Mn^{2+}, Mg^{2+} phosphors for advanced X-ray imaging applications.

2 Experiment

The Zn_2SiO_4 host and Zn_2SiO_4:x%Mn^{2+},y%Mg^{2+} samples were synthesized via a high-temperature solid-phase reaction. The flexible film containing polydimethylsiloxane (PDMS) and Zn_2SiO_4:0.3%Mn^{2+},0.4%Mg^{2+} powders is denoted as the Zn_2SiO_4:Mn^{2+},Mg^{2+}@PDMS film. Similarly, the film based on BGO powders is denoted as the BGO@PDMS film. Further details of preparation are provided in Part A of the ESM (Fig. S1 in the ESM).

3 Results and discussion

3.1 Characteristics of crystal structures

As shown in Fig. 1(a), the Zn_2SiO_4 host crystallizes in a rhombohedral structure with a $R\bar{3}$ space group, and the lattice constants of the unit cell are $a = b$ = 13.939 Å and c = 9.309 Å. In the unit cell, each Zn and Si atom is coordinated by four oxygen atoms, forming [ZnO_4] and [SiO_4] tetrahedra, respectively. By comparing r of each atom with the same coordination number (CN), Mg^{2+} (CN = 4, r = 0.57 Å) and Mn^{2+} (CN = 4, r = 0.66 Å) tend to substitute for Zn^{2+} (CN = 4, r = 0.60 Å) rather than for Si^{4+} (CN = 4, r = 0.26 Å).

The X-ray diffraction (XRD) patterns of Zn_2SiO_4 host, Zn_2SiO_4:x%Mn^{2+}, and Zn_2SiO_4:0.3%Mn^{2+},y%Mg^{2+} samples are shown in Fig. 1(b) and Fig. S2 in the ESM. All diffraction peaks are in good agreement with the standard card (PDF#37-1485) of Zn_2SiO_4 host, suggesting high phase purity of synthesized samples. It should be noted that the diffraction peak shifts from 34.00° to 33.88° due to the lattice expansion caused by Mn^{2+}–Zn^{2+} substitution (Fig. 1(b)). However, when co-doped with Mg^{2+}, the peak shifts slightly back to a larger angle of 33.93°, indicating a contraction of lattice structure. Figures S2(c)–S2(e) in the ESM present the Rietveld refinements (based on primitive cell) of Zn_2SiO_4 host, Zn_2SiO_4:0.3%Mn^{2+}, and Zn_2SiO_4:0.3%Mn^{2+}, 0.4%Mg^{2+} samples. The low weighted R-factors (R_{wp} < 15%) and profile R-factors (R_p) indicate that no significant impurities were introduced by the substitution of Zn^{2+} with Mn^{2+} or Mg^{2+}. To investigate the modifying effect of Mg^{2+} on the crystal lattice, the refined lattice parameters and B-factor—an indicator of structural rigidity—are summarized in Table S2 in the ESM. Upon Mn doping, the lattice parameters a and b show slight increases, while c increases notably from 8.623 to 8.630 Å, resulting in an expansion of primitive cell volume from 522.243 to 522.871 Å^3. Meanwhile, the B-factor rises from 1.81 to 2.14 Å^2, indicating reduced structural rigidity after Mn^{2+} doping. The more pronounced variation along the c-axis can be attributed to the intrinsic anisotropy of Zn_2SiO_4 [37]. With Mg^{2+} co-doping, both a and b contract slightly, and c significantly shrinks back from 8.630 to 8.624 Å. The calculated volume contracts to 522.440 Å^3, with B-factor correspondingly decreasing to 2.01 Å^2. The Rietveld refinement results confirm that Mg^{2+} co-doping effectively modifies the expanded crystal lattice and restores lattice rigidity.

As shown in the scanning electron microscopy (SEM) images (Fig. 1(c)), the particles of Zn_2SiO_4:0.3%Mn^{2+},0.4%Mg^{2+} sample exhibit irregular shapes with diameters of approximately 10 μm. Elemental mapping confirmed the homogeneous distribution of Zn, Si, O, Mn, and Mg in the prepared samples (Fig. 1(d)). The valence state of Mn, which is closely related to its luminescent properties, was determined by X-ray photoelectron spectroscopy (XPS) analysis (Fig. 1(e)). The XPS signals could be fitted with two peaks centered at 653.8 and 643.9 eV, corresponding to the $2p_{3/2}$ and $2p_{1/2}$ orbitals of Mn^{2+}, respectively [38]. Notably, no significant XPS signal corresponding to Mn^{4+} was observed in the spectra, indicating that Mn predominantly exists as Mn^{2+} in all prepared samples. As shown in Fig. S3 in the ESM, the band gap (E_g) of Zn_2SiO_4 host is 4.3 eV, as determined from the diffuse reflection spectra of Zn_2SiO_4 host (Fig. S3(a) in the ESM) [39].

The photoluminescence excitation (PLE) spectra of the Zn_2SiO_4:0.3%Mn^{2+} sample, monitored at 525 nm emission, exhibit a peak at 37784 cm^{-1} (~265 nm) (Fig. 2(a)). This PLE spectra can be deconvoluted into two subordinate peaks. Peak 1, centered at 37,734 cm^{-1} (~280 nm), originates from the Mn^{2+}–O^{2-} charge transfer band (CTB) [40,41]. Peak 2, centered at 40,007 cm^{-1}

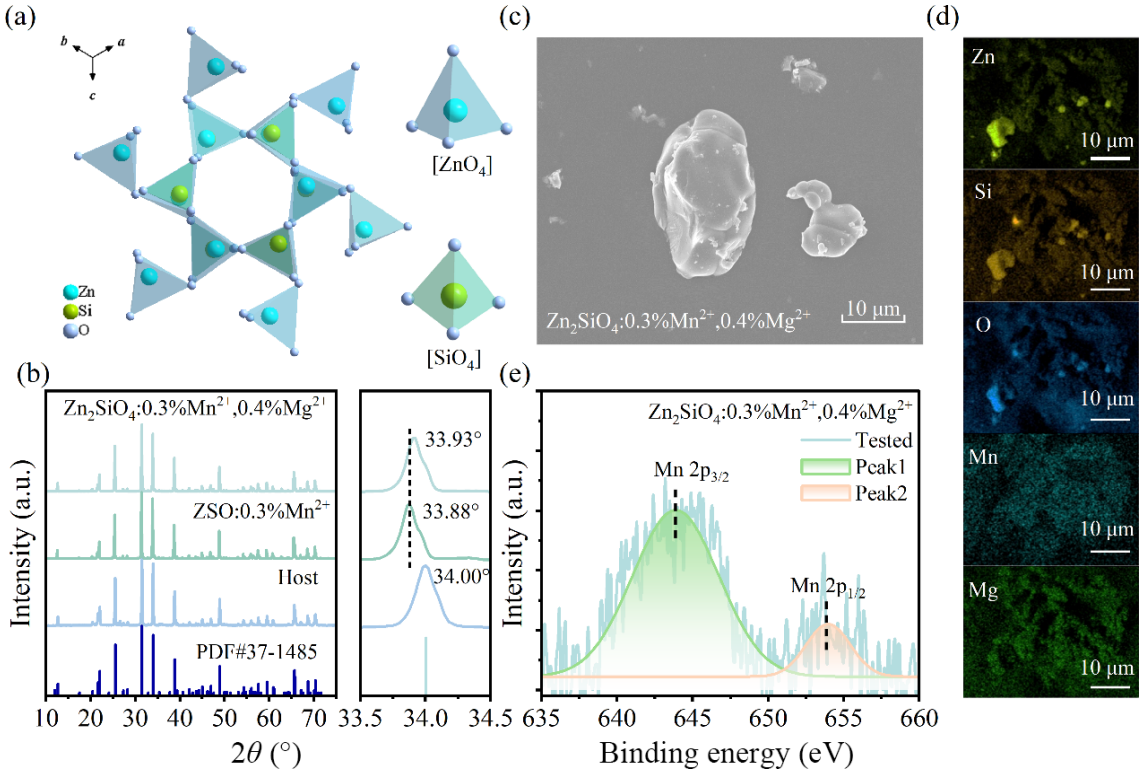

Fig. 1 (a) Crystal structure of Zn_2SiO_4. (b) XRD patterns of the Zn_2SiO_4 host, Zn_2SiO_4:0.3%Mn^{2+}, and Zn_2SiO_4:0.3%Mn^{2+},0.4%Mg^{2+} samples, with the standard card (PDF#37-1485) given as a reference. (c) SEM image of the Zn_2SiO_4:0.3%Mn^{2+},0.4%Mg^{2+} sample. (d) Elemental mapping of Zn, Si, O, Mn, and Mg in the Zn_2SiO_4:0.3%Mn^{2+},0.4%Mg^{2+} sample. (e) XPS signal of Mn^{2+} in Zn_2SiO_4:0.3%Mn^{2+},0.4%Mg^{2+}.

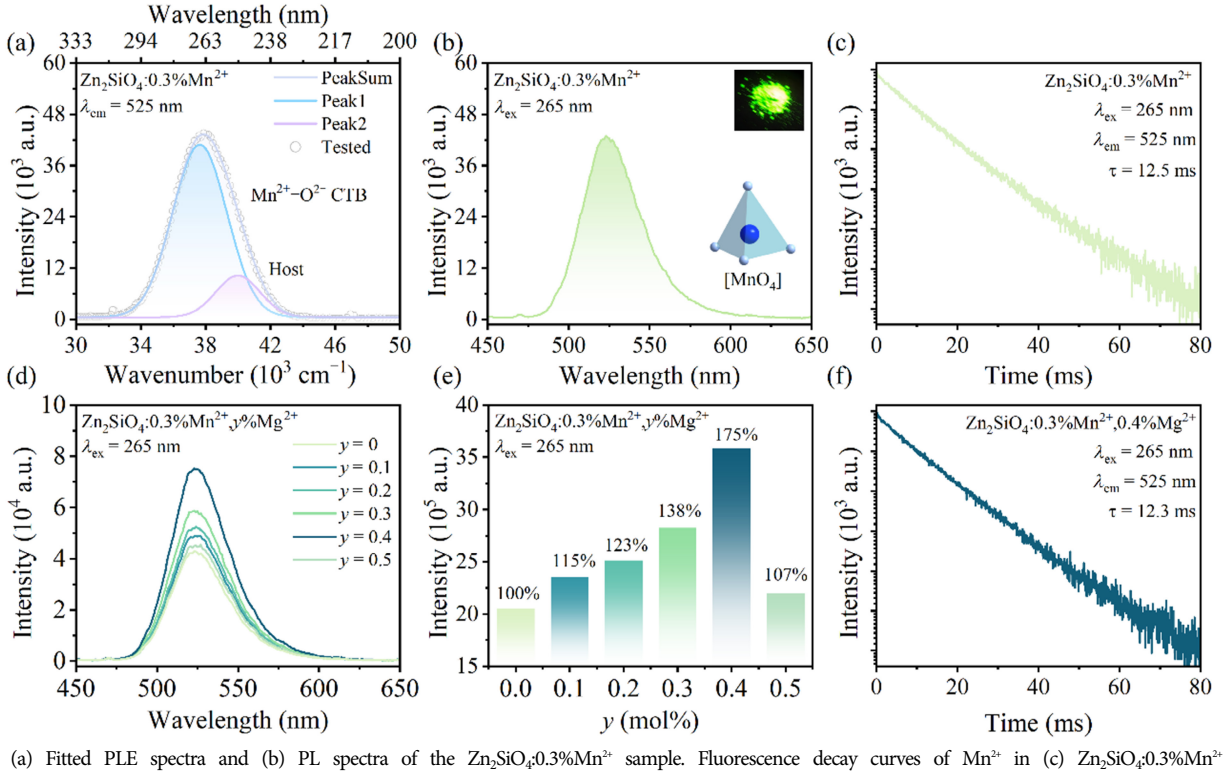

Fig. 2 (a) Fitted PLE spectra and (b) PL spectra of the Zn_2SiO_4:0.3%Mn^{2+} sample. Fluorescence decay curves of Mn^{2+} in (c) Zn_2SiO_4:0.3%Mn^{2+} and (f) Zn_2SiO_4:0.3%Mn^{2+},0.4%Mg^{2+} samples. (d) PL spectra and (e) PL integrated intensity of Zn_2SiO_4:0.3%Mn^{2+},*y*%Mg^{2+} samples under 265 nm excitation.

(~250 nm), is attributed to the absorption of energy by the host lattice [41]. As shown in Fig. 2(b), the PL spectra of Zn_2SiO_4:0.3%Mn^{2+} sample (λ_{ex} = 265 nm) exhibit a single emission peak centered at 19,047 cm^{-1} (525 nm), which corresponds to the $^4T_1 \rightarrow {}^6A_1$ energy transition of Mn^{2+} within the [MnO_4] tetrahedron [42,43]. The inset illustrates the coordination environment of Mn^{2+} and shows a real luminescent image of Zn_2SiO_4:0.3%Mn^{2+} sample.

According to the concentration optimization of Mn^{2+}, Zn_2SiO_4:0.3%Mn^{2+} sample was determined to be the optimal sample for PL (Fig. S4 in the ESM). The fluorescence decay curve

of Zn_2SiO_4:0.3%Mn^{2+} sample at an emission wavelength of 536 nm was measured under 325 nm excitation (Fig. 2(c)). The average lifetime (τ) of T_1 state of Mn^{2+} was then calculated using Eq. (1) [39]:

$$\tau = \frac{\int tI(t)\mathrm{d}t}{\int I(t)\mathrm{d}t} \quad (1)$$

where $I(t)$ denotes the emission intensity of the sample at time t. The calculated τ value for Zn_2SiO_4:0.3%Mn^{2+} sample is 12.5 ms, which is characteristic of the typical d-d forbidden transition of Mn^{2+}. This suitable τ value indicates negligible afterglow and a low nonradiative relaxation process for Mn^{2+} in Zn_2SiO_4:0.3%Mn^{2+} sample [44–46]. In addition, the concentration quenching of Mn^{2+} was further investigated using Stern–Volmer model, and it was found to be dominated by an exchange interaction mechanism (Figs. S5(a) and S5(b) in the ESM) [47,48].

Generally, the luminescence of Mn^{2+} can also be affected by various defects within materials, such as structural defects, anion/cation vacancies, antisite defects, and interstitial defects [49,50]. In this context, structural defects include local lattice distortion, which may be induced by the substitution of ions with different ionic radii. During equivalent substitution, structural defects play an important role in influencing the lattice structure [50,51]. In this work, the ionic radius of Mn^{2+} (CN = 4, r = 0.66 Å) is slightly larger than that of Zn^{2+} (CN = 4, r = 0.60 Å). The equivalent substitution of Mn^{2+} for Zn^{2+} may therefore lead to lattice expansion, which can introduce structural defects and subsequently cause luminescence quenching.

To compensate for the local lattice expansion induced by Mn^{2+}, a smaller Mg^{2+} (CN = 4, r = 0.57 Å) was intentionally incorporated into Zn_2SiO_4:0.3%Mn^{2+} sample. The PL spectra (λ_{ex} = 265 nm) of Zn_2SiO_4:0.3%Mn^{2+},y%Mg^{2+} samples are shown in Fig. 2(d). Upon Mg^{2+} co-doping, the emission peak of Mn^{2+} exhibits no significant shift, whereas the PL intensity is remarkably improved. As the Mg^{2+} concentration increases, the integrated PL intensity first increases monotonically and then decreases (Fig. 2(e)), reaching an optimum at a Mg^{2+} concentration of 0.4%. For Zn_2SiO_4:0.3%Mn^{2+},0.4%Mg^{2+} sample, the integrated PL intensity reaches 175% of that of Zn_2SiO_4:0.3%Mn^{2+} sample. In addition, compared with Zn_2SiO_4:0.3%Mn^{2+} sample, the average lifetime of Mn^{2+} slightly shortens as Mg^{2+} concentration increases from 0.1 to 0.4 mol% (Fig. 2(f) and Fig. S5(c) in the ESM). This slight reduction may be ascribed to the increased radiative transition probability resulting from lattice modification induced by Mg^{2+} incorporation [20,52]. However, when the Mg^{2+} exceeds 0.4 mol%, the average lifetime of Mn^{2+} decreases significantly, which is also consistent with the results shown in Fig. 2(e). These findings demonstrate that Mg^{2+} incorporation effectively improves the luminescence of Mn^{2+}. This enhancement can be attributed to the reduction in lattice defects caused by Mg^{2+} incorporation, which will be further discussed in Section 3.2.

3.2 Thermal stability and thermoluminescence studies

The temperature-dependent PL spectra (λ_{ex} = 265 nm) of Zn_2SiO_4:0.3%Mn^{2+} and Zn_2SiO_4:0.3%Mn^{2+},0.4%Mg^{2+} samples were measured over the temperature range of 303–563 K at intervals of 20 K (Fig. 3(a) and 3(b)). For both samples, the peak position of the PL spectra remains nearly unchanged with increasing temperature. In Zn_2SiO_4:0.3%Mn^{2+} sample, the full width at half maximum (FWHM) monotonically broadens from 40.8 to 54.0 nm as the temperature rises, which is attributed to the electron–phonon coupling effect (Figs. 3(c) and 3(d), Table S3 in the ESM) [53]. However, upon Mg^{2+} incorporation, the broadening degree is reduced (from 40.4 to 53.0 nm, i.e., a 12.6 nm broadening vs. 13.2 nm for the undoped one), which is attributed to a decrease in the electron-phonon coupling strength, resulting from the enhanced structural rigidity induced by Mg^{2+} co-doping [54]. Consequently, the Commission Internationale de l'Éclairage (CIE) coordinates of the two samples exhibit only a slight

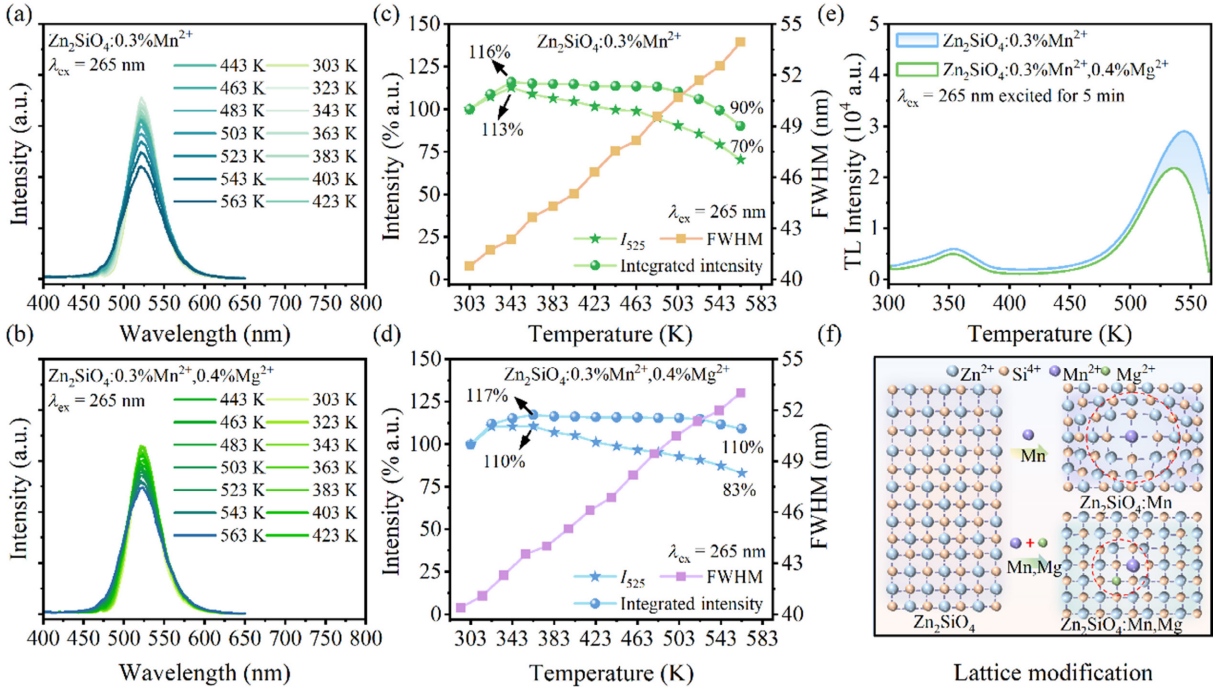

Fig. 3 Temperature-dependent PL spectra of (a) Zn_2SiO_4:0.3%Mn^{2+} and (b) Zn_2SiO_4:0.3%Mn^{2+},0.4%Mg^{2+} samples. Temperature-dependent integrated intensity (I_{525}) and FWHM of (c) Zn_2SiO_4:0.3%Mn^{2+} and (d) Zn_2SiO_4:0.3%Mn^{2+},0.4%Mg^{2+} samples. (e) TL glow curve of Zn_2SiO_4:0.3%Mn^{2+} and Zn_2SiO_4:0.3%Mn^{2+},0.4%Mg^{2+} samples after 5 min excitation at 265 nm. (f) Lattice modification induced by Mg^{2+} doping in Zn_2SiO_4:Mn^{2+}.

deviation, as shown in Fig. S6 in the ESM [24,55]. Furthermore, the effect of Mg^{2+} incorporation on the thermal stability of Mn^{2+} luminescence is evaluated in detail. Compared with the values at 303 K, the integrated intensity of Zn_2SiO_4:0.3%Mn^{2+} sample initially increases to 116% at 343 K and then decreases to 90% at 563 K, while the peak intensity (I_{525}) reaches 113% at 343 K and drops to 70% at 563 K (Fig. 3(c)). However, upon Mg^{2+} incorporation, Zn_2SiO_4:0.3%Mn^{2+},Mg^{2+} sample exhibits improved thermal stability. Compared with the values at 303 K, its integrated PL intensity reaches 117% at 363 K and decreases to 83% at 563 K, while its I_{525} reaches 110% at 363 K and remains 110% at 563 K (Fig. 3(d)). These results indicate that Mg^{2+} co-doping effectively improves the thermal stability of Mn^{2+}, achieving anti-thermal quenching in PL. These values are superior to those of many reported Mn^{2+}-based materials (Table 1).

To investigate the effect of Mg^{2+} on structural defects, thermoluminescence (TL) curves of Z_2SiO_4:0.3%Mn^{2+} and Z_2SiO_4:0.3%Mn^{2+},0.4%Mg^{2+} samples were measured (Fig. 3(e)). The two samples were pre-excited using a 265 nm LED for 5 min, and the TL curves were recorded at a heating rate of 1 K/s. As shown in Fig. 3(e), the TL curves of two samples exhibit similar shapes. It should be noted that compared with Z_2SiO_4:0.3%Mn^{2+} sample, the TL intensity of Z_2SiO_4:0.3%Mn^{2+}, 0.4%Mg^{2+} sample is relatively weaker (Fig. S7 and Table S4 in the ESM). Obviously, upon Mg^{2+} co-doping, the nonradiative recombination defects in Z_2SiO_4:0.3%Mn^{2+}, 0.4%Mg^{2+} sample are effectively suppressed, while the radiative recombination defects are preserved. As a result, the luminescence and high thermal stability of Mn^{2+} are significantly improved [60,61].

According to the above findings, a reasonable mechanism for lattice modification is proposed, as illustrated in Fig. 3(f). For the Z_2SiO_4:0.3%Mn^{2+} sample, Zn^{2+} is substituted by Mn^{2+} during the high-temperature solid-phase reaction. Since the ionic radius of Mn^{2+} is larger than that of Zn^{2+}, this substitution may induce lattice expansion in the crystal structure. When Mg^{2+} is co-doped, the replacement of Zn^{2+} by smaller Mg^{2+} leads to size compensation and modifies the local lattice structure around Mn^{2+} (Fig. 3(f)). This compensation reduces nonradiative recombination defects, thereby enhancing radiative recombination and increasing lattice rigidity [25]. In addition, the higher lattice rigidity weakens electron-phonon coupling, which improves the thermal stability of Mn^{2+} and reduces the degree of FWHM broadening. However, when the Mg^{2+} concentration is excessively high, local lattice contraction may introduce new structural defects, resulting in re-suppression of Mn^{2+} luminescence, as shown in Fig. 2(e).

3.3 Scintillation performance

The above findings confirm the beneficial effect of Mg^{2+} on the PL properties of Mn^{2+}. Inspired by previous reports summarized in Table S1 in the ESM, the scintillation performance of Zn_2SiO_4:Mn^{2+},Mg^{2+} was then further explored. Accordingly, the effect of Mg^{2+} on the XEL intensity of Mn^{2+} and the scintillation potential of the Zn_2SiO_4:0.3%Mn^{2+},0.4%Mg^{2+} sample were then specifically investigated. As shown in Fig. S8 in the ESM, the good stopping efficiency of Zn_2SiO_4:0.3%Mn^{2+},0.4%Mg^{2+} sample is demonstrated by its X-ray absorption coefficient.

To determine the sample with optimal scintillation performance, the concentrations of Mn^{2+} and Mg^{2+} were then systematically optimized. As shown in Fig. S9 in the ESM, the optimal Mn^{2+} concentration is 0.3 mol%. Upon the incorporation of Mg^{2+}, the integrated XEL intensity of Mn^{2+} also shows a significant enhancement, which first increases and then decreases with rising Mg^{2+} concentration (Fig. 4(a)). The highest XEL intensity is observed in Zn_2SiO_4:0.3%Mn^{2+},0.4%Mg^{2+} sample, reaching 493% of that of BGO powders and 2 times higher than that of Zn_2SiO_4:0.3%Mn^{2+} sample. This outstanding performance is comparable to that of many reported Mn^{2+}-doped scintillators (Table 2).

Subsequently, the thermal stability of Mn^{2+} with and without Mg^{2+}, was investigated under X-ray irradiation from 303 to 483 K (Fig. S10(a) in the ESM and Fig. 4(b)). The FWHM values of both samples broaden from approximately 42 to 53 nm (Fig. S10(b) and Table S5 in the ESM), accompanied by slight deviations in the CIE coordinates (Fig. S11 in the ESM). As the temperature rises from 303 to 483 K, the integrated XEL intensity and the I_{525} at 483 K for Zn_2SiO_4:0.3%Mn^{2+} remain at 105% and 86% of their respective values at 303 K (Fig. S10(c) in the ESM). Such thermal stability can be further improved with the incorporation of Mg^{2+}. The integrated XEL intensity and I_{525} of Zn_2SiO_4:0.3%Mn^{2+},0.4%Mg^{2+} samples show a monotonic increase, reaching 126% and 104% (at 483 K) of their respective values at 303 K (Fig. S10(d) in the ESM). This outstanding thermal stability of Mn^{2+} is superior to that of many reported materials listed in Table 1. According to the TL analysis (Fig. S12 in the ESM), this anomalous behavior can also be attributed to lattice modification induced by Mg^{2+} incorporation, which is consistent with the results shown in Figs. 3(c) and 3(d). In addition, the excitation energy of X-rays is much higher than that of ultraviolet light. Under X-ray irradiation, the excited electrons fill more trap centers (Figs. S7 and S12 in the ESM). Upon heating, the release of these trapped electrons compensates for luminescence loss,

Table 1 Comparison of thermal stability of reported Mn^{2+}-based materials under ultraviolet and X-ray irradiation

Material	Type	Thermal stability	Ref.
$Cs_3Cu_2I_5$:Mn	Metal halide	71% at 433 K (XEL)	[43]
Cs_3MnBr_5	Nanocrystal	73% at 563 K (XEL)	[56]
$[TPPen]_2Mn_{0.9}Zn_{0.1}Br_4$	Hybrid halide	85% at 383 K (XEL)	[5]
SiO_2–CaF_2–NaF–Al_2O_3:Mn^{2+}	Glass	61% at 573 K (XEL)	[46]
$ETTP_2MnCl_4$	Hybrid halide	112% at 403 K (XEL)	[7]
$Gd_3(Al,Ga)_5O_{12}$:Ce^{3+},Mn^{2+}	Crystal	35% at 393 K (PL)	[2]
$NaY_9(SiO_4)_6O_2$:Mn^{2+}	Phosphors	95% at 423 K (PL)	[57]
$NaMg_{2.5}Mn_{0.5}AlSi_3O_{10}F_2$	Ceramics	78% at 423 K (PL)	[58]
$(BPTP)_2MnBr_4$	Metal halide	60.3% at 403 K (PL)	[59]
$ZnAl_2O_4$:Mn^{2+}	Phosphors	60% at 423 K (PL)	[20]
Z_2SiO_4:Mn^{2+},Mg^{2+}	Phosphors	110% at 563 K (PL)	This work
Z_2SiO_4:Mn^{2+},Mg^{2+}	Phosphors	126% at 483 K (XEL)	This work

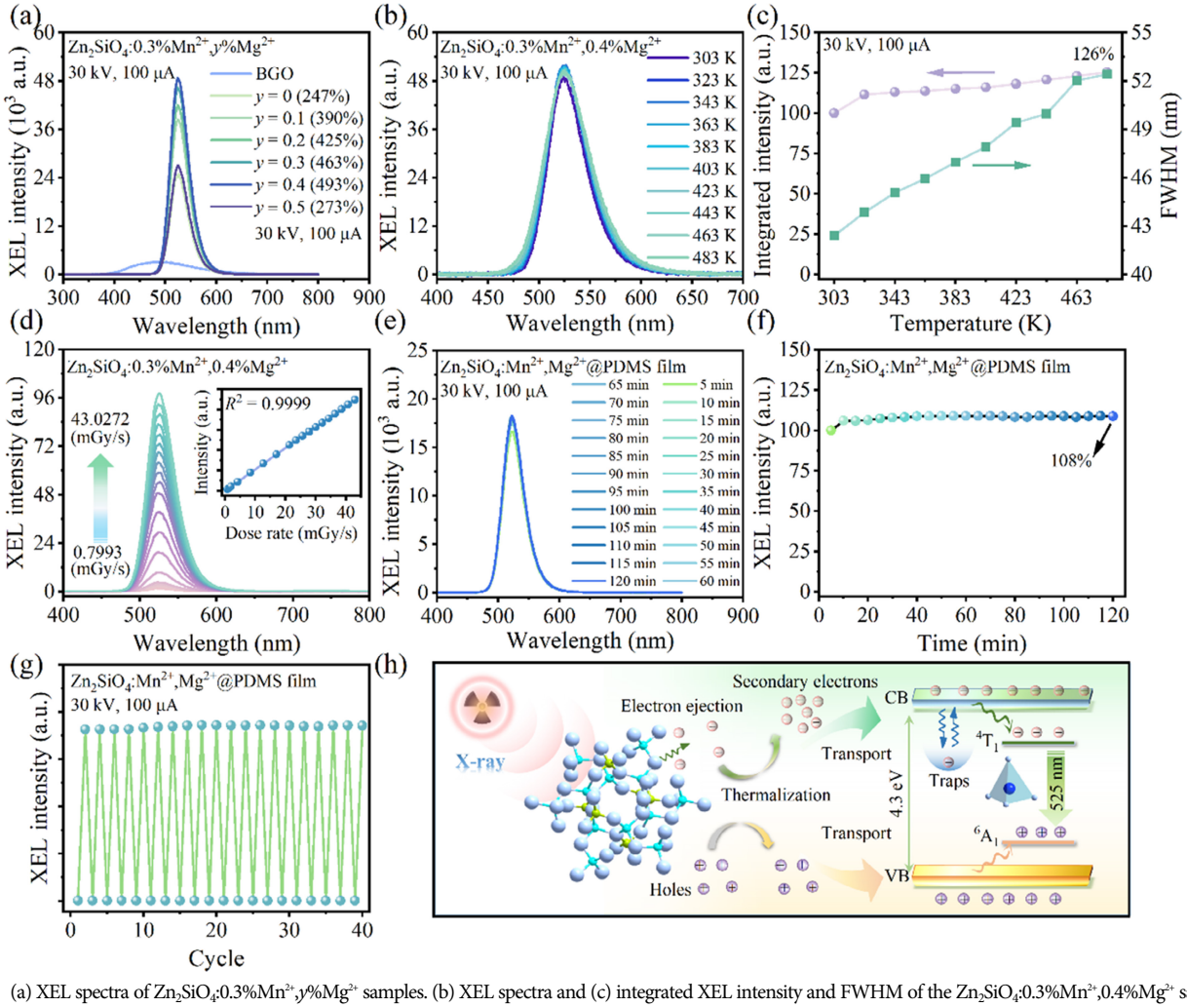

Fig. 4 (a) XEL spectra of Zn_2SiO_4:0.3%Mn^{2+},*y*%Mg^{2+} samples. (b) XEL spectra and (c) integrated XEL intensity and FWHM of the Zn_2SiO_4:0.3%Mn^{2+},0.4%Mg^{2+} sample at different temperatures. (d) XEL spectra of Zn_2SiO_4:0.3%Mn^{2+},*y*%Mg^{2+} samples under different dose rates. (e) XEL spectra and (f) integrated XEL intensity of the Zn_2SiO_4:Mn^{2+},Mg^{2+}@PDMS film under prolonged X-ray irradiation. (g) Corresponding XEL intensity measured over 20 on/off irradiation cycles. (h) XEL mechanism.

Table 2 Comparison of XEL intensity and X-ray imaging resolution among reported Mn^{2+}-doped scintillators

Material	Type	I_{XEL}	Resolution (lp/mm)	Ref.
$Gd_3(Al,Ga)_5O_{12}:Ce^{3+},Mn^{2+}$	Crystal	351%	20	[2]
Cs_3MnBr_5	Metal halide	52%	19.1	[56]
$[TPPen]_2Mn_{0.9}Zn_{0.1}Br_4$	hybrid halide	680%	11.2	[5]
SiO_2–CaF_2–NaF–Al_2O_3:Mn^{2+}	Glass	83.6%	20	[46]
SiO_2–Al_2O_3–BaF_2–NaF:Cu^{+}	Glass	311%	24	[11]
NaF–Al_2O_3–SiO_2–SrF_2:Cu^{+}	Glass	425%	20	[8]
$CsMnCl_3$	Nanocrystal	156%	4.3	[62]
$Cs_2CdBr_2Cl_2$:Mn^{2+}	Perovskite	—	12.3	[4]
$ETPP_2MnCl_4$	Hybrid halide	200%	12.2	[7]
Lu_2WO_6:Eu^{3+}	Phosphor	—	18.2	[63]
$LuYO_3$:Eu^{2+}	Phosphor	—	11	[64]
Zn_2SiO_4:Mn^{2+}	Phosphor	493%	20	This work

Note: I_{XEL} — the ratio of the XEL intensity of the reported materials to that of commercial BGO.

resulting in a monotonic increase in XEL intensity over the temperature range of 303–483 K.

The XEL spectra and integrated XEL intensity of Zn_2SiO_4:0.3%Mn^{2+},0.4%Mg^{2+} samples were then measured at different X-ray dose rates. The sample exhibits an excellent linear response coefficient to X-rays (R^2 = 0.9999), indicating its promising scintillation potential (see the insert of Fig. 4(d)).

To better evaluate the scintillation potential, a Zn_2SiO_4:Mn^{2+},Mg^{2+}@PDMS film was prepared via the spin-coating method, which has not been previously reported [30,31,36] (Fig. S1 and Table S1 in the ESM). As shown in Figs. S13(a)–S13(d) in the ESM, the prepared film, with a thickness of 0.50 mm, retains both the original structure and the luminescent properties of Zn_2SiO_4:0.3%Mn^{2+},0.4%Mg^{2+} powders.

Generally, material structures may be damaged by continuous X-ray irradiation, leading to a decline in luminescent intensity. Therefore, the X-ray resistance of $Zn_2SiO_4:Mn^{2+},Mg^{2+}$@PDMS film was then examined. As shown in Fig. 4(e), the film was exposed to continuous X-ray irradiation for 120 min, and its XEL spectra were recorded at 5-min intervals. Figure 4(f) presents the integrated XEL intensity at different irradiation times. The integrated XEL intensity initially increased during the first 5 min of irradiation, an effect known as "bright burn effect". According to TL analysis (Fig. S12 in the ESM), this effect is attributed to competitive capture of excited electrons by luminescent centers and trap centers within the material. As the irradiation time increases, trap centers are gradually filled. Consequently, more excited electrons are captured by the luminescent centers, resulting in a rapid enhancement of the XEL intensity during the first 5 min of X-ray irradiation (Fig. 4(f)). Once the trap centers are completely filled, all excited electrons are captured by the luminescent centers, and the XEL intensity stabilizes with prolonged irradiation time, remaining at 108% of the initial intensity. The excellent X-ray on/off cycling stability of the film is shown in Fig. 4(g), demonstrating the sustainable applicability of $Zn_2SiO_4:Mn^{2+},Mg^{2+}$@PDMS film under continuous irradiation.

In addition, the film also exhibits outstanding physicochemical stability. After immersion in CH_3CH_2OH and H_2O for 10 d, the PL intensities of $Zn_2SiO_4:Mn^{2+},Mg^{2+}$@PDMS film remained at 96.1% and 97.0%, respectively (Fig. S14 in the ESM), while the XEL intensities remained at 98.3% and 97.0%, respectively (Fig. S15 in the ESM). These results confirm the potential application of $Zn_2SiO_4:Mn^{2+},Mg^{2+}$@PDMS film under prolonged exposure to moisture and extreme environmental conditions.

Considering the above findings, a possible luminescent mechanism is proposed, as shown in Fig. 4(h). Upon X-ray irradiation, X-ray photons interact with the heavy atoms in the material via the photoelectric effect and Compton scattering. Subsequently, numerous high-energy electrons and holes are generated and thermalized. Most of these secondary carriers are transported to the conduction band (CB) and valence band (VB), where they are captured by Mn^{2+}, enabling radiative relaxation from the $^4T_1$ to $^6A_1$ energy level. Meanwhile, a small fraction of the secondary electrons is captured by trap centers within the phosphor, resulting in a "bright burn effect" during the first 5 min of irradiation. As the temperature rises, the trapped electrons are thermally released, compensating for the luminescent loss. Consequently, Zn_2SiO_4:0.3%Mn^{2+},0.4%Mg^{2+} sample exhibits exceptional anti-thermal quenching luminescence under X-ray irradiation.

3.4 Applications

Beyond the fundamental studies previously reported for this system (Table S1 in the ESM), the practical X-ray imaging performance of $Zn_2SiO_4:Mn^{2+},Mg^{2+}$@PDMS film was then investigated using a self-constructed imaging system (Fig. 5(a)). Figure 5(b) shows pictures of the prepared film under daylight (left) and under X-ray irradiation (right). For X-ray imaging, the internal structure of a chip (Fig. 5(c)) can be clearly observed in the X-ray image in air (Fig. 5(d1)). Moreover, the same structural features remain clearly visible when the object is immersed in water at a depth of 1 cm (Fig. 5(d2)). Modulation transfer function (MTF) analysis indicates that the theoretical spatial resolution of $Zn_2SiO_4:Mn^{2+},Mg^{2+}$@PDMS film is 22.5 lp/mm

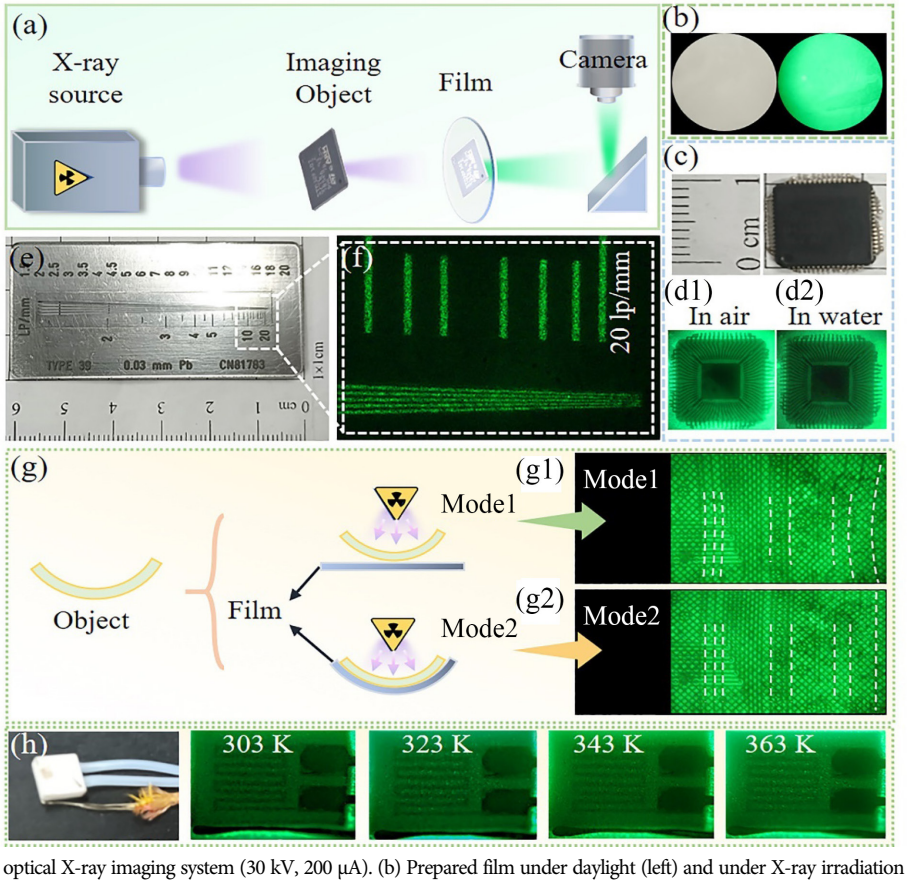

Fig. 5 (a) Self-assembled optical X-ray imaging system (30 kV, 200 μA). (b) Prepared film under daylight (left) and under X-ray irradiation (right). (c) Pictures of the chip under daylight. (d1, d2) X-ray images of the chip in air and in water. (e) Picture of the resolution test standard line pair card under daylight, and (f) under X-ray irradiation. (g) Illustration of flexible X-ray imaging using a flexible printed circuit: mode 1—traditional projection method; mode 2—flexible film attachment method. (h) X-ray images of the heating chip at different temperatures.

(Fig. S17 in the ESM). The experimental spatial resolution, measured using a standard line-pair card (Fig. 5(e)), reaches 20 lp/mm both in air and underwater (Fig. S16 in the ESM). This value is comparable to those of many reported scintillators, as listed in Table 2.

Generally, the flexibility of the scintillation film offers a unique advantage in imaging fields with complex curved surfaces (Fig. 5(g)). Here, a flexible printed circuit was used as the imaging object and was attached to the scintillation film in two different contact modes. In mode 1, the X-ray images of the printed circuit are significantly distorted, as indicated by the white dashed line (Fig. 5(g1)). This suggests that the traditional projection method is not suitable for X-ray imaging of curved surfaces. In mode 2 (Fig. 5(g2)), the original structure of the circuit can be clearly observed without deformation (white dashed line). This result confirms the unique value of flexible film attachment method for complex curved objects. Considering the anti-thermal quenching property of Zn_2SiO_4:Mn^{2+},Mg^{2+} sample under X-ray irradiation, a chip was used to further estimate the X-ray imaging stability of the prepared film at high temperatures. As shown in Fig. 5(h), the internal structure of the chip can be resolved even at 363 K. The X-ray image becomes slightly blurred, which is attributed to the reversible softening of PDMS and the increased fluidity of the powder at high temperatures. The X-ray images of the chip during heating at 303 (original), 363 (heated), and 303 K (cooling down) are depicted in Fig. S18 in the ESM. These results demonstrate the remarkable thermal stability and sustainability of Zn_2SiO_4:Mn^{2+},Mg^{2+}@PDMS film in X-ray imaging applications.

4 Conclusions

Therefore, in addition to the PL property, this work demonstrates that Mg^{2+} incorporation can also enhance thermal stability and scintillation performance. For Zn_2SiO_4:0.3%Mn^{2+},0.4%Mg^{2+} sample, its integrated PL and XEL intensities are enhanced to 1.75 and 2 times, respectively, compared with those of Zn_2SiO_4:0.3%Mn^{2+} sample. Its PL and XEL intensities exhibit exceptional anti-thermal quenching behavior, retaining 110% (PL, at 563 K) and 126% (XEL, at 483 K) of their initial intensities at 303 K. In addition, Zn_2SiO_4:Mn^{2+},Mg^{2+} sample shows a high XEL intensity (493% of that of BGO) with a perfect linear X-ray response. It also exhibits a high spatial resolution of 20 lp/mm with excellent physicochemical stability in H_2O and CH_3CH_2OH. TL analysis reveals that Mg^{2+} incorporation effectively suppresses nonradiative recombination defects through lattice modification. This study may contribute to the research on Zn_2SiO_4:Mn^{2+} and provide an effective approach to developing novel scintillators for advanced X-ray imaging.

Acknowledgements

This work was supported by the National Natural Science Foundation of China (Grant No. 12574443).

Author contributions

Simin Yu: Investigation and writing–original draft; Guanlin He: Investigation; Xinglin Jiang: Investigation; Hai Guo: Conceptualization, resources, writing–review & editing, and supervision.

Availability of data and materials

The data that support the findings of this study are available from the corresponding author upon reasonable request.

Competing interests

The authors have no competing interests to declare that are relevant to the content of this article. The author Hai Guo is the Editorial Committee member of this journal.

Electronic Supplementary Material

Supplementary material is available in the online version of this article at https://doi.org/10.26599/JAC.2026.9221352.

References

[1] Yang SY, Zhang L, Kong FC, *et al.* Scintillators with aggregation-induced emission. *Chem* 2025, **11**: 102534.
[2] Zhang AC, Li MQ, Li CY, *et al.* Mn–Ce co-activated garnet crystals as bright scintillators for fast gamma and high-performance X-ray imaging. *Chem Eng J* 2025, **515**: 163235.
[3] Hu C, Zhu DY, Wang YB, *et al.* Defect engineering in Mg^{2+} co-doped LuAG:Ce ceramics: Towards ultrahigh fast scintillation proportion. *J Adv Ceram* 2025, **14**: 9221148.
[4] Xu HP, Liang WQ, Zhang ZZ, *et al.* 2D perovskite Mn^{2+}-doped $Cs_2CdBr_2Cl_2$ scintillator for low-dose high-resolution X-ray imaging. *Adv Mater* 2023, **35**: 2300136.
[5] Jin JC, Han K, Hu YK, *et al.* Zn^{2+} doping in organic manganese(II) bromide hybrid scintillators toward enhanced light yield for X-ray imaging. *Adv Opt Mater* 2023, **11**: 2300330.
[6] Wang Y, Zhang P, Tian X, *et al.* Persistent scintillators for X-ray repetitive imaging with stable energy traps. *J Rare Earths* 2025, **43**: 1161–1168.
[7] Jin SL, Huang QX, Wei LY, *et al.* A thermally robust organic–inorganic hybrid scintillator enabled by RISC-assisted Mn^{2+} emission for high-temperature X-ray imaging. *Laser Photonics Rev* 2026, **20**: 01917.
[8] He GL, Li LJ, Chen JY, *et al.* A thermal stable multi-functional Cu^{+}-doped glass for high-resolution X-ray imaging and full-spectra lighting. *Laser Photonics Rev* 2025, **19**: 00396.
[9] Li LJ, Chen JY, He GL, *et al.* Tb^{3+}-doped phosphors-based-glass scintillators with excellent performance for high-temperature X-ray imaging. *Laser Photonics Rev* 2026, **20**: 02368.
[10] Pan JW, Lei JH, Wei RF, *et al.* Eu^{2+}-doped transparent glass–ceramics with superior scintillation performance and stability for high-resolution X-ray imaging. *Laser Photonics Rev* 2026, **20**: 01906.
[11] He GL, Chen JY, Li LJ, *et al.* Cu^{+}-doped oxyfluoride glass with anti-thermal-quenching luminescence for X-ray imaging and WLED. *J Adv Ceram* 2025, **14**: 9221116.
[12] Salway H, Chua XW, Anaya M. Metal–organic frameworks as potential materials for X-ray detectors: Recent progress and unique opportunities. *Mater Horiz* 2025, **12**: 8989–9008.
[13] Yang ZJ, Chen C, He Y, *et al.* Advances in nanocrystal scintillators for X-ray imaging and biomedical applications. *CCS Chem* 2025, **7**: 3553–3568.
[14] Martin-Monier L, Pajovic S, Abebe MG, *et al.* Large-scale self-assembled nanophotonic scintillators for X-ray imaging. *Nat Commun* 2025, **16**: 5750.
[15] Chen JH, Luo JB, He ZL, *et al.* An anti-thermal-quenching organic–inorganic hybrid manganese-based single-crystal scintillator for high-temperature X-ray imaging. *Chem Sci* 2025, **16**: 9375–9384.
[16] Xu L, Ran P, Zhou WQ, *et al.* All-inorganic metafabric scintillators for conformally flexible and wearable X-ray detection and imaging. *Sci Adv* 2025, **11**: 5537.
[17] Wang T, Hu S, Ji T, *et al.* High-temperature X-ray imaging with transparent ceramics scintillators. *Laser Photonics Rev* 2024, **18**: 2300892.
[18] Fan JL, Li HB, Liu W, *et al.* Fabrication strategies of Mn^{2+}-based scintillation screens for X-ray detection and imaging. *Angew Chem Int Ed* 2025, **64**: 202425661.
[19] Rong H, Xu XQ, Yao JY, *et al.* High-resolution flexible X-ray imaging in a two-dimensional Mn^{2+}-doped perovskite scintillator. *ACS Appl Mater Interfaces* 2025, **17**: 24137–24145.
[20] Zhan CY, Zhu HM, Liang SS, *et al.* Mn^{2+}–Mn^{2+} dimers induced robust light absorption in heavy Mn^{2+} doped $ZnAl_2O_4$ near-infrared

phosphor with an excellent photoluminescence quantum yield and thermal stability. *Adv Opt Mater* 2024, **12**: 2400574.
[21] Wang YJ, Pan X, Liu ZQ, *et al.* Self-reduction-induced Mn heterovalent coexistence for vis–NIR dual-emission. *J Adv Ceram* 2025, **14**: 9221118.
[22] Cong L, Lv LY, Liu Y, *et al.* Manganese halides with timely and delayed reversible thermal fluorescence quenching for dual-secure information encryption and anti-counterfeiting. *Chem Eng J* 2025, **505**: 159672.
[23] Wang F, Lv PF, Xiao GJ, *et al.* Abnormal blueshift of Mn d–d emission unlocked by decreasing phonon coupling under high pressure. *Angew Chem Int Ed* 2025, **64**: 202500318.
[24] Gao JL, Guo YY, Zhang XH, *et al.* Phonon involved photoluminescence of Mn^{2+} ions doped $CsPbCl_3$ micro-size perovskite assembled crystals. *Adv Sci* 2025, **12**: 2413402.
[25] Krasnenko TI, Zaitseva NA, Ivanova IV, *et al.* The effect of Mg introduction on structural and luminescence properties of Zn_2SiO_4: Mn phosphor. *J Alloys Compd* 2020, **845**: 156296.
[26] Zhang P, Jiang XY, Gao JY, *et al.* Layered-tunnel structure enables high defect tolerance for coexistence of anomalous thermal quenching and mechanoluminescence in $Sr_2ZnSi_2O_7:Mn^{2+}$. *Mater Today Phys* 2026, **60**: 101958.
[27] Dong LP, Zhang L, Jia YC, *et al.* Site occupation and luminescence of novel orange-red $Ca_3M_2Ge_3O_{12}:Mn^{2+},Mn^{4+}$ (M = Al, Ga) phosphors. *ACS Sustainable Chem Eng* 2020, **8**: 3357–3366.
[28] Dolecsek G, Bulancea-Lindvall O, Davidsson J, *et al.* Native defects and impurities in talcum quasi-2D layers. *npj 2D Mater Appl* 2025, **9**: 97.
[29] Dolado J, Martínez-Casado R, Hidalgo P, *et al.* Understanding the UV luminescence of zinc germanate: The role of native defects. *Acta Mater* 2020, **196**: 626–634.
[30] Jarý V, Vařák P, Babin V, *et al.* Scintillation properties of zinc-silicate glass-ceramics based on Zn_2SiO_4 willemite phase. *Opt Mater* 2025, **162**: 116961.
[31] Diana P, Sivaganesh D, Sivakumar V, *et al.* UV-induced photoluminescence and X-ray-induced thermoluminescence of Zn_2SiO_4:Mn phosphor. *J Mater Sci Mater Electron* 2023, **34**: 1992.
[32] Reshchikov MA. Mechanisms of thermal quenching of defect-related luminescence in semiconductors. *Phys Status Solidi A* 2021, **218**: 2000101.
[33] Linderälv C, Åberg D, Erhart P. Luminescence quenching via deep defect states: A recombination pathway via oxygen vacancies in Ce-doped YAG. *Chem Mater* 2021, **33**: 73–80.
[34] Dazai T, Yasui S, Taniyama T, *et al.* Cation-deficiency-induced crystal-site engineering for $ZnGa_2O_4:Mn^{2+}$ thin film. *Inorg Chem* 2020, **59**: 8744–8748.
[35] Wu YP, Wu M, Yang SW, *et al.* Cation occupation engineering realizes valence modulation of manganese-activated $ZnGa_2O_4$. *ACS Appl Mater Interfaces* 2024, **16**: 35342–35352.
[36] Ivanova IV, Krasnenko TI. Analysis of the reasons for the enhanced green luminescence of Mg^{2+}-doped $Zn_2SiO_4:Mn^{2+}$ phosphor. *Opt Mater* 2024, **157**: 116261.
[37] Perkins HK, Sienko MJ. ESR study of manganese-doped α-zinc silicate crystals. *J Chem Phys* 1967, **46**: 2398–2401.
[38] Li ZF, Zhang WJ, Xin CY, *et al.* Multi-color luminescent material with Mn^{2+}/Mn^{4+} non-stoichiometric ratio doped octahedra and its anti-counterfeiting applications. *Ceram Int* 2024, **50**: 18043–18052.
[39] Feng MJ, Guo JJ, Chen JY, *et al.* Four-mode optical thermometry based on Sm^{3+}-doped Lu_2WO_6 self-activated phosphors. *J Rare Earths* 2025, **43**: 1812–1820.
[40] Feng P, Wang YH, Ding SS. Theoretical calculations and investigation on properties and defect states in $SrMgGe_2O_6:Mn^{2+}$, Sm^{3+}. *Chem Eng J* 2022, **450**: 137820.
[41] Yu SM, Gong YJ, He GL, *et al.* Multimodal luminescence of $CaZnGe_2O_6:Mn^{2+}$, Yb^{3+} phosphors for anti-counterfeiting: Dynamic photoluminescence, afterglow, photostimulated luminescence, thermostimulated luminescence and mechanoluminescence. *Chem Eng J* 2025, **524**: 169152.
[42] Wang CY, Li YC, Deng ZT. Emission-tunable manganese(ii) halides: Structure–property relationships and functional applications. *Chem Sci* 2025, **16**: 15796–15814.
[43] Li XM, Chen JX, Yang DD, *et al.* Mn^{2+} induced significant improvement and robust stability of radioluminescence in $Cs_3Cu_2I_5$ for high-performance nuclear battery. *Nat Commun* 2021, **12**: 3879.
[44] Fox M, *Optical properties of solids*, Oxford (UK): Oxford University Press, 2010.
[45] Liu SY, Fang XY, Lu B, *et al.* Wide range zero-thermal-quenching ultralong phosphorescence from zero-dimensional metal halide hybrids. *Nat Commun* 2020, **11**: 4649.
[46] Li LJ, Su QQ, Chen JY, *et al.* Mn^{2+}-doped glass scintillators with anti-thermal quenching for high-temperature X-ray imaging. *Chin Opt Lett* 2025, **23**: 111602.
[47] Lin C, Dienes A. Study of excitation transfer in laser dye mixtures by direct measurement of fluorescence lifetime. *J Appl Phys* 1973, **44**: 5050–5052.
[48] Ito A, Stewart DJ, Knight TE, *et al.* Excited-state dynamics in rigid media: Evidence for long-range energy transfer. *J Phys Chem B* 2013, **117**: 3428–3438.
[49] Xiao Y, Xiong PX, Zhang S, *et al.* Cation-defect-induced self-reduction towards efficient mechanoluminescence in Mn^{2+}-activated perovskites. *Mater Horiz* 2023, **10**: 3476–3487.
[50] Wu L, Sun SJ, Bai YX, *et al.* Defect-induced self-reduction and anti-thermal quenching in $NaZn(PO_3)_3:Mn^{2+}$ red phosphor. *Adv Opt Mater* 2021, **9**: 2100870.
[51] Tang YQ, Cai YY, Dou KP, *et al.* Dynamic multicolor emissions of multimodal phosphors by Mn^{2+} trace doping in self-activated $CaGa_4O_7$. *Nat Commun* 2024, **15**: 3209.
[52] Xiao Y, Yang X, Zhao HR, *et al.* Tracing the origin of near-infrared emissions emanating from manganese (II). *Light Sci Appl* 2025, **14**: 194.
[53] Shen XR, Kong JF, Wang FC, *et al.* Temperature-dependent Mn^{2+} emission in codoped $CsPb_2(BrCl)_5$ perovskite nanocrystals. *Opt Express* 2024, **32**: 34920.
[54] Medrish IV, Eremin RA, Blatov VA. From simple to complex: Design of inorganic crystal structures with a topologically extended zintl–klemm concept. *J Phys Chem Lett* 2020, **11**: 8114–8120.
[55] van Bunningen AJ, Sontakke AD, van der Vliet R, *et al.* Luminescence temperature quenching in Mn^{2+} phosphors. *Adv Opt Mater* 2023, **11**: 2202794.
[56] Le YK, Huang XJ, Zhang H, *et al.* Transparent glassy composites incorporating lead-free anti-perovskite halide nanocrystals enable tunable emission and ultrastable X-ray imaging. *Adv Photon* 2023, **5**: 046002.
[57] Zeng QF, Runowski M, Xue JP, *et al.* Pressure-induced remarkable spectral red-shift in Mn^{2+}-activated $NaY_9(SiO_4)_6O_2$ red-emitting phosphors for high-sensitive optical manometry. *Adv Sci* 2024, **11**: 2308221.
[58] Jiang MR, Qi N, Mao YF, *et al.* Realizing intense deep-far-red broadband emission derived from mica ceramics through isomorphic cation substitution/doping for plant cultivation lighting and latent fingerprint identification. *J Adv Ceram* 2026, **15**: 9221254.
[59] Zhang RQ, Xie HD, Liu W, *et al.* High-efficiency narrow-band green-emitting manganese(II) halide for multifunctional applications. *ACS Appl Mater Interfaces* 2023, **15**: 47238–47249.
[60] Li JP, Tu ZY, Zheng YK, *et al.* Zero-thermal-quenching and charge compensation for efficient luminescence in $Ca_9ZnK(PO_4)_7:Sm^{3+}$: Optimizing defect engineering. *Ceram Int* 2024, **50**: 9869–9877.
[61] Pan X, Mei LF, Zhuang YX, *et al.* Anti-defect engineering toward high luminescent efficiency in whitlockite phosphors. *Chem Eng J* 2022, **434**: 134652.
[62] Li K, Zhang WC, Niu LY, *et al.* Lead-free cesium manganese halide nanocrystals embedded glasses for X-ray imaging. *Adv Sci* 2023, **10**: 2204843.
[63] Zhang SA, Li ZZ, Ye HC, *et al.* Data mining evoking scintillators auto-discovery for low-LoD high-resolution deep-penetrating X-ray imaging of portable digital radiography. *Adv Funct Mater* 2025, **35**: 2415220.
[64] Fan PP, Li MX, Zhao X, *et al.* Energy-resolved color X-ray imaging via stacked ultra-narrowband scintillators for material discrimination. *Mater Today* 2026, **92**: 339–346.